Supplementary Information

Pogo-Stick Iron and Cobalt Complexes: Synthesis, Structures and Magnetic Properties

Marius Peters, Dirk Baabe, Miyuki Maekawa, Dirk Bockfeld, Marc-Kevin Zaretzke, Matthias Tamm,* Marc D. Walter*

Institut für Anorganische und Analytische Chemie, Technische Universität Braunschweig, Hagenring 30, 38106 Braunschweig, Germany

Table of Contents

S1 Synthesis and analysis of [Cp'$_2$Co]

1-Co (750 mg, 0.894 mmol) was dissolved in toluene (15 mL) and a suspension of NaCp' (459 mg, 1.79 mmol, 2 equiv.) in toluene (5 mL) was added. The mixture was heated to 120 °C overnight, while the color changed from red-brown to brown-black. The solvent was removed, the residue extracted with *n*-hexane, filtered and the solvent was removed. The oily residue was distilled under reduced pressure at 120 °C and the obtained solid was redissolved in diethylether (3 mL) and stored at –35 °C. The target compound was obtained as a dark black-red crystalline solid. Yield: 47 mg (0.09 mmol, 5 %). Single crystals for X-ray diffraction analysis were grown from a concentrated *n*-hexane solution at –35 °C.

^{1}H NMR (300.1 MHz, C_6D_6): δ = 3.65 (s, br, 18H, C(CH_3)$_3$, $\nu_{1/2}$ = 19 Hz), 3.47 (s, br, 36H, C(CH_3)$_3$, $\nu_{1/2}$ = 86 Hz) ppm.

The obtained values agree with the spectroscopic data from the literature.[1] Both signals overlap, but deconvolution of these overlapping resonances made a full assignment possible.

S2 NMR spectroscopy

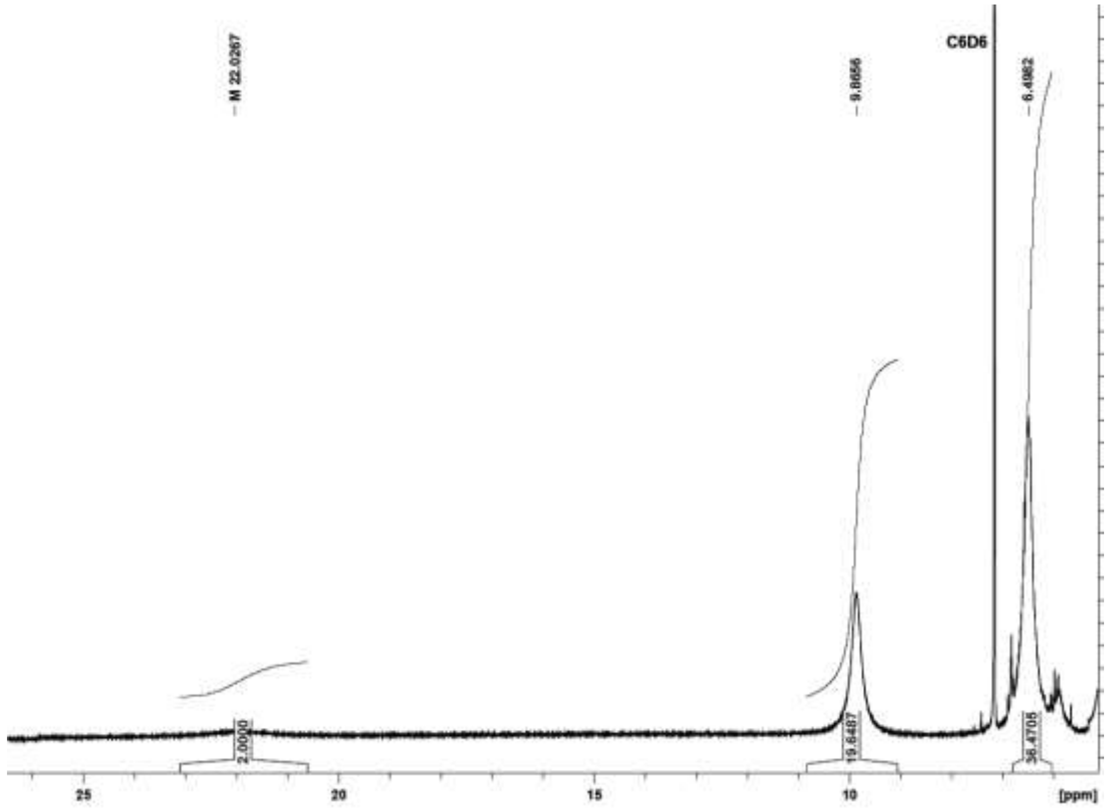

Figure S1. [1]H NMR spectrum of **1-Co** in C_6D_6.

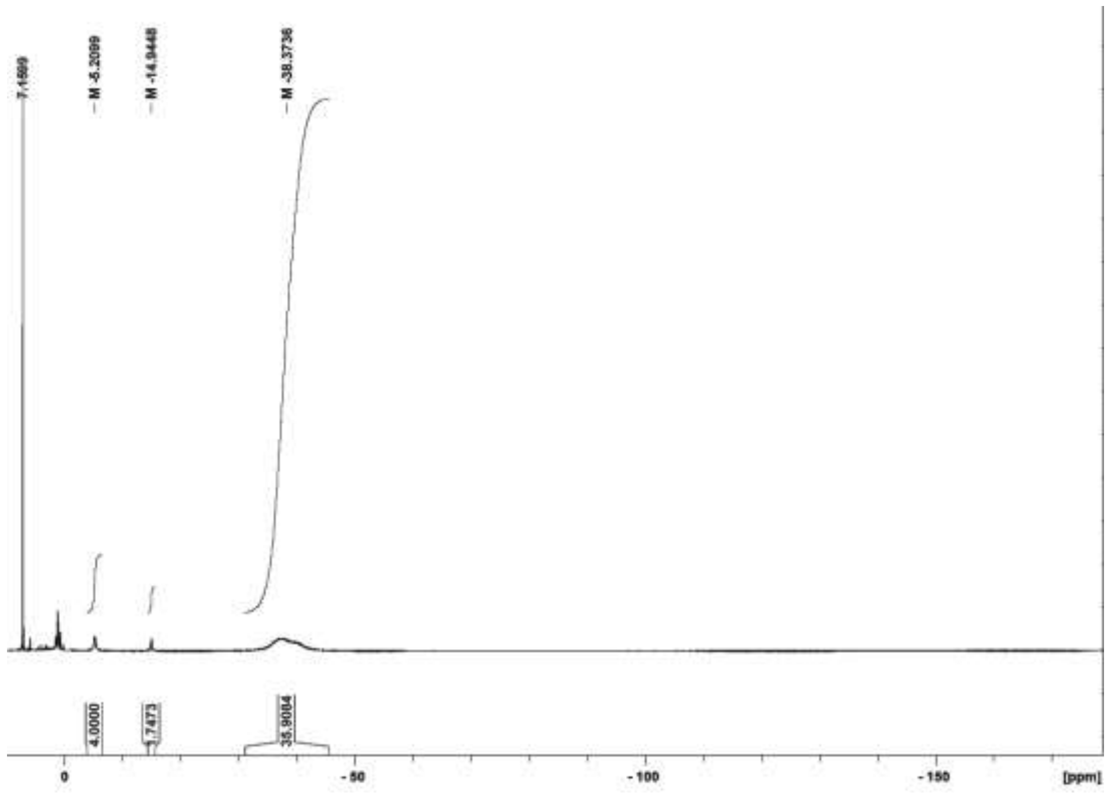

Figure S2. [1]H NMR spectrum of **2-Fe** in C_6D_6 (range 1).

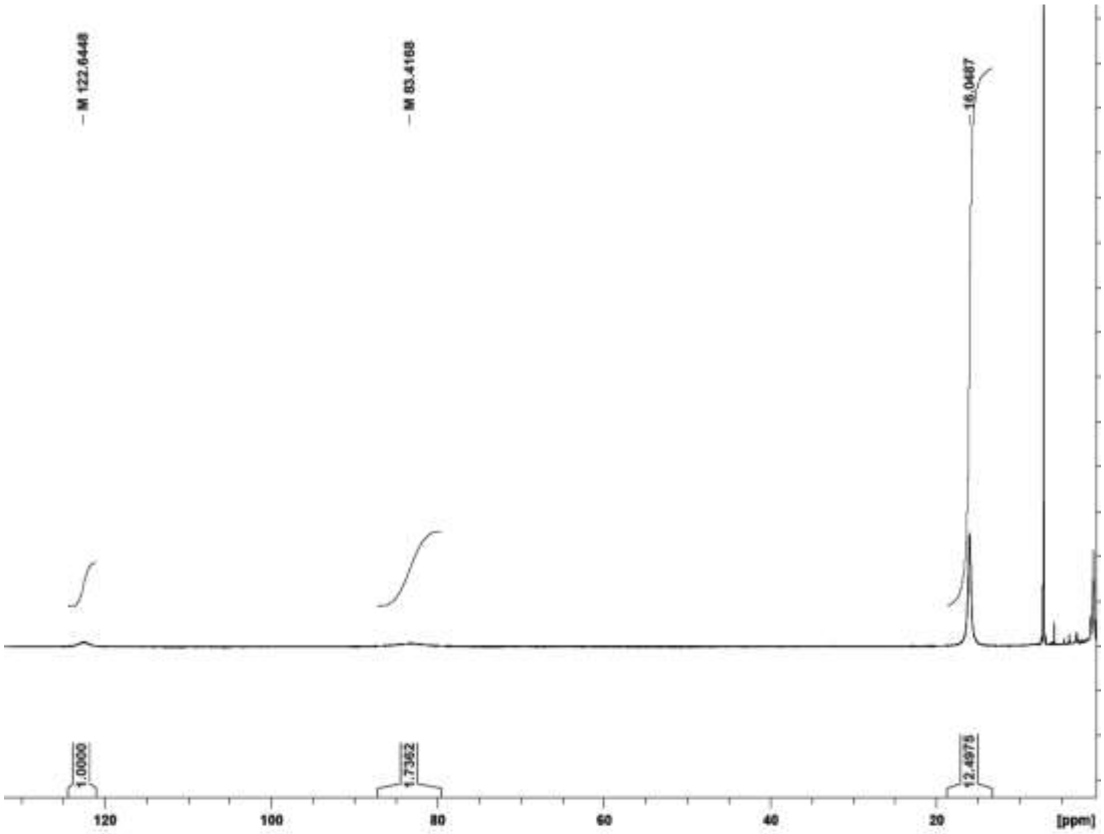

Figure S3. [1]H NMR spectrum of **2-Fe** in C_6D_6 (range 2).

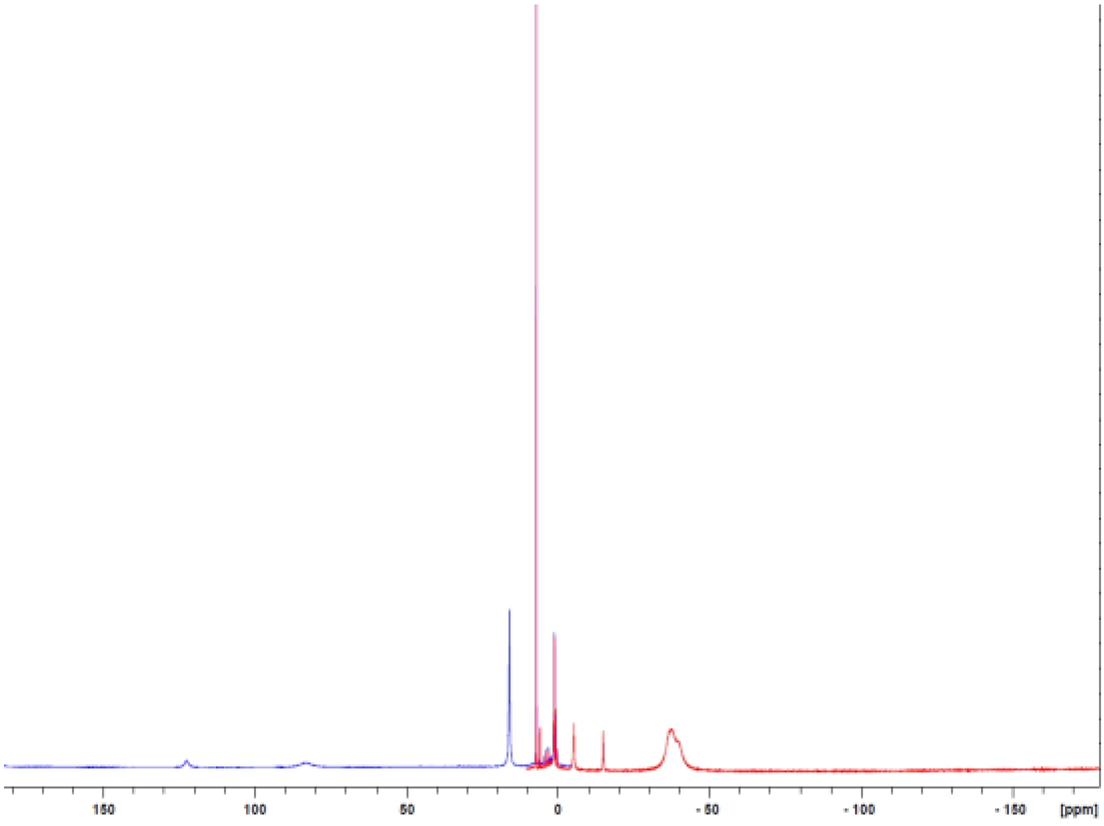

Figure S4. [1]H NMR spectrum of **2-Fe** in C_6D_6.

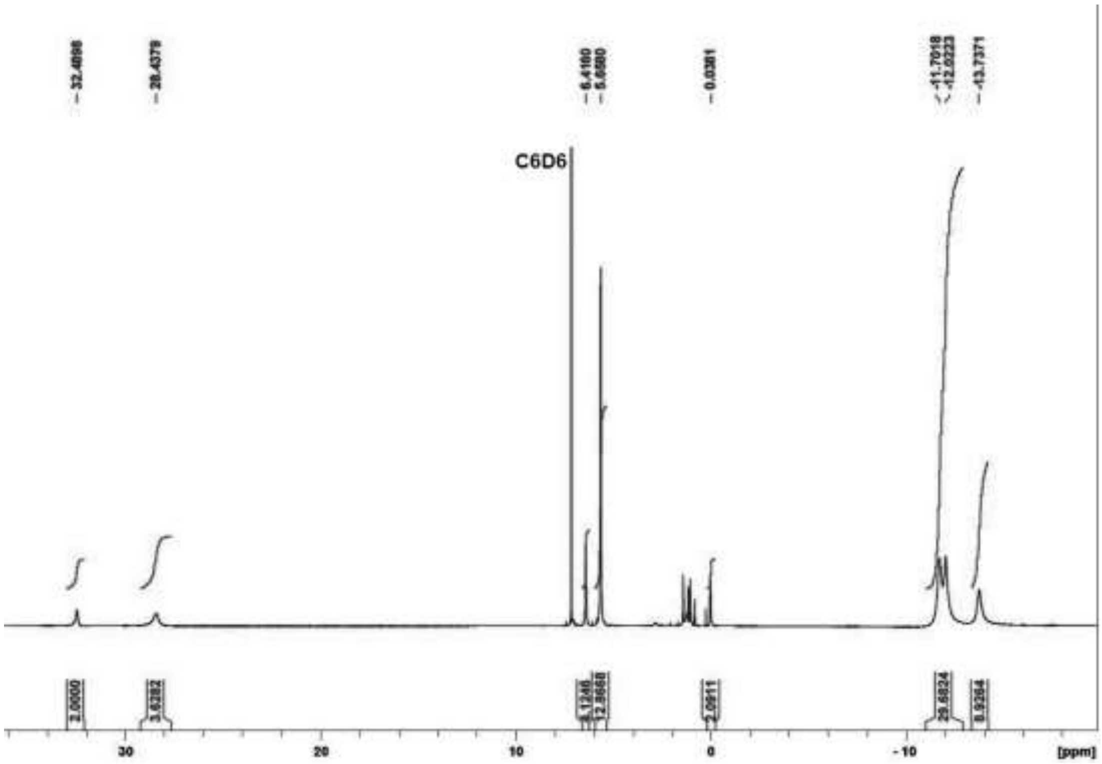

Figure S5. ^{1}H NMR spectrum of **2-Co** in C_6D_6.

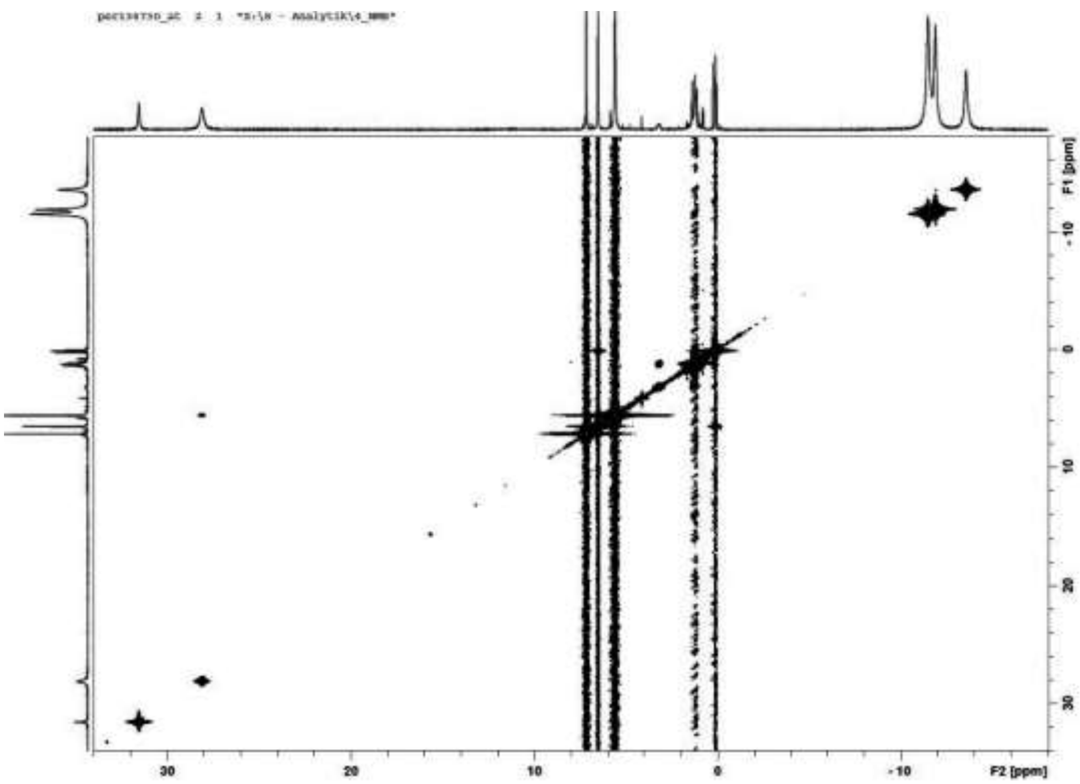

Figure S6. ^{1}H,^{1}H-COSY NMR spectra of **2-Co** in C_6D_6.

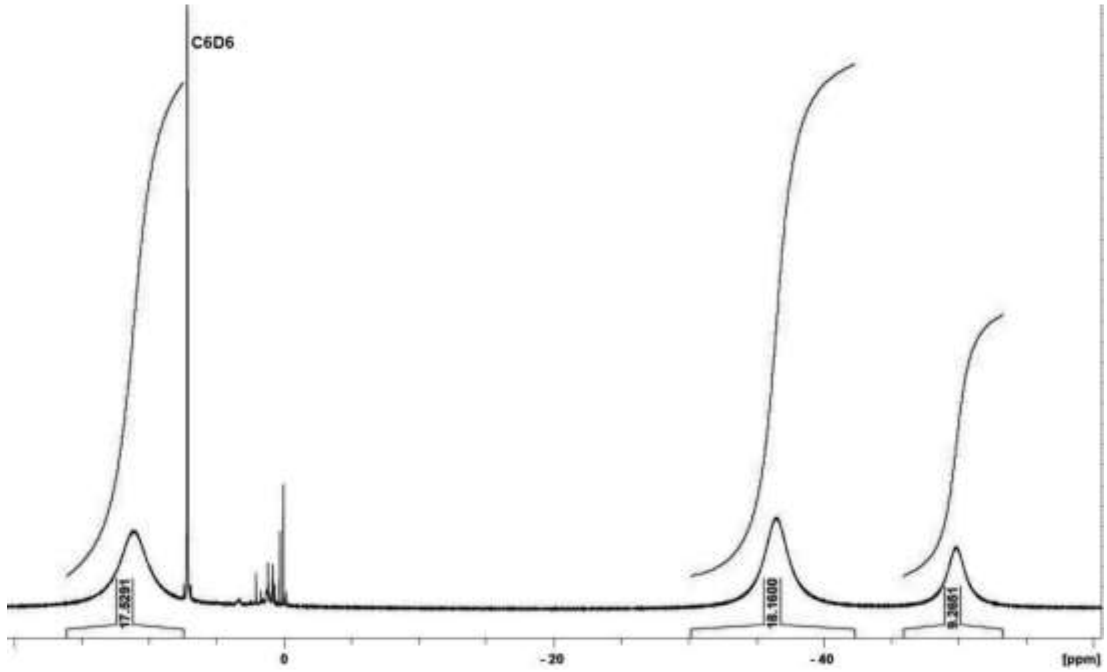

Figure S7. [1]H NMR spectrum of **3-Co** in C_6D_6.

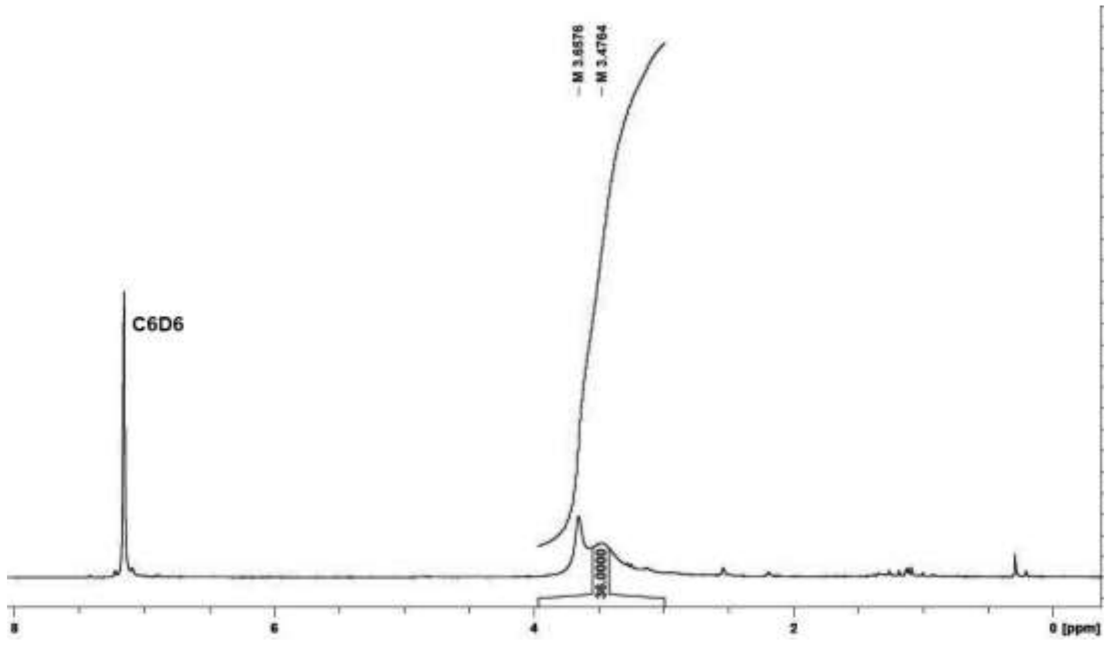

Figure S8. [1]H NMR spectrum of [Cp'$_2$Co] in C_6D_6.

S3 Single crystal X-ray diffraction

The crystals were either prepared on MiTeGen mounts (**2-Fe** (100 K and 250 K), [Cp'$_2$Co]) or on top of a human hair (**2-Co** (273 K), **3-Co**) or a glass needle (**1-Co**, **2-Co** (100 K)) with perfluorinated inert oil. Data were recorded on Rigaku XtaLAB Synergy S Single Source diffractometers equipped with a PhotonJet Cu-microfocus source (**2-Co** (273K)) or a PhotonJet Mo-microfocus source ([Cp'$_2$Co], **2-Fe** (100 K and 250 K)) and a HyPix-6000HE detector. Data collections for **1-Co** and **2-Co** (100 K) were performed on an Oxford Diffraction Xcalibur E diffractometer equipped with a Mo-finefocus X-ray tube and an Eos CCD detector. Single crystals of **3-Co** were measured on an Oxford Diffraction Xcalibur Nova diffractometer with a Cu-microfocus X-ray source and an Atlas CCD detector. Data reduction was performed with CrysalisPro[2] (versions: **1-Co**: 1.171.35.21 (**2012**), **2-Co** (100 K), **3-Co**: 1.171.38.43 (**2015**), [Cp'$_2$Co], **2-Co** (273 K): 1.171.40.39a (**2019**), **2-Fe** (100 K and 250 K): 1.171.40.45a (**2019**), Rigaku Corporation, Oxford, UK.). Absorption correction was based on multi-scans and additionally face indexation and integration on a Gaussian grid was applied for all compounds except **1-Co**. All structures except **1-Co** were solved by intrinsic phasing with SHELXT[3] and refined on F^2 using the program SHELXL[4] in OLEX2[5] ([Cp'$_2$Co], **2-Co** (273 K), **3-Co**, **2-Fe** (100 K and 250 K)) or WinGX[6] (**2-Co** (100 K)). The structure of **1-Co** was solved with direct methods in SHELXS-97[7] and refined on F^2 using the program SHELXL[4] in SHELXTL.[8] All H atoms were placed in idealized positions and refined using a riding model.

Data collection at elevated temperatures for compounds **2-Co** (273 K) and **2-Fe** (250 K) resulted in higher thermal motion leading to B-level alerts in the respective checkcif files associated with the shape and size of the thermal ellipsoids.

The dataset of [Cp'$_2$Co] contained a small number of reflections, which were affected by the beamstop and some intensities were not measured correctly. Therefore, the corresponding reflections were omitted. Overall only 31 of *ca.* 30000 reflections are missing resulting in a B-level alert in the checkcif file.

Table S1. Crystal structure data

Compound	**1-Co**	**2-Fe**	**2-Fe**	**2-Co**	**2-Co**	**3-Co**	[Cp'$_2$Co]
CCDC	1942611	1942612	1942613	1942614	1942615	1942616	1942617
Formula	$C_{34}H_{58}Co_2I_2$	$C_{44}H_{65}FeN_3$	$C_{44}H_{65}FeN_3$	$C_{44}H_{65}CoN_3$	$C_{44}H_{65}CoN_3$	$C_{23}H_{47}CoNSi_2$	$C_{34}H_{58}Co$
M_r	838.46	691.84	691.84	694.92	694.92	452.72	525.73
Habit	brown/dark-turquoise dichroic block	irregular (red)	irregular (red)	irregular (brown)	irregular (brown)	plate (brown)	block (brown)
Cryst. size (mm)	0.30 x 0.20 x 0.10	0.75 x 0.42 x 0.31	0.76 x 0.44 x 0.33	0.60 x 0.29 x 0.10	0.15 x 0.10 x 0.05	0.16 x 0.11 x 0.04	0.47 x 0.23 x 0.13
Crystal system	monoclinic	monoclinic	monoclinic	monoclinic	triclinic	monoclinic	monoclinic
Space group	$P2_1/c$	$P2_1/c$	$P2_1/c$	$P2_1/c$	P-1	$C2/c$	$P2_1/c$
Temperature (°C)	–173	–173	–23	–173	0	–173	–173
Cell constants:							
a (Å)	13.9563(3)	21.7096(5)	22.0003(7)	21.4167(18)	10.8678(7)	17.7514(3)	18.4537(5)
b (Å)	18.6294(2)	10.3922(2)	10.4491(2)	10.4125(6)	19.6952(7)	15.2854(3)	17.1831(5)
c (Å)	15.1111 (2)	20.5125(5)	20.7099(6)	20.1162(14)	19.9478(7)	19.7812(3)	19.5406(5)
α (°)	90	90	90	90	84.267(3)	90	90
β (°)	115.551(2)	116.704(3)	117.344(4)	114.928(8)	83.388(4)	91.1680(10)	90.980(2)
γ (°)	90	90	90	90	87.094(4)	90	90
V (Å^3)	3544.59(5)	4134.23(19)	4228.9(2)	4068.0(6)	4216.8(3)	5366.26(16)	6195.3(3)
Z	4	4	4	4	4	8	8
D_x (Mg m^{-3})	1.571	1.112	1.087	1.135	1.095	1.121	1.127
μ (mm^{-1})	2.698	0.396	0.387	0.454	3.407	5.905	0.573
F(000)	1688	1504	1504	1508	1508	1976	2312
λ (Å)	0.71073	0.71073	0.71073	0.71073	1.54184	1.54184	0.71073
$2\theta_{max}$	61.88	58.258	58.260	57.400	133.202	152.494	72.636
Refl. measured	253662	143763	147921	101609	80800	42105	227458
Refl. indep.	10847	11123	11395	10498	14863	5613	29998
R_{int}	0.0481	0.0350	0.0316	0.0702	0.1785	0.0654	0.0293
Parameters	361	450	450	450	898	259	667
Restraints	0	0	0	0	0	0	0
$wR2(F^2$, all refl.)	0.0228	0.0957	0.1488	0.1139	0.2976	0.0868	0.0742
$R1(F, >4\sigma(F))$	0.0440	0.0345	0.0496	0.0445	0.0988	0.0330	0.0263
S	1.070	1.036	1.049	1.036	1.021	1.028	1.042
max.$\Delta\rho$ (e Å^{-3})	0.856 / –0.683	0.826 / –0.535	0.551 / –0.507	0.574 / –0.663	1.082 / –0.612	0.247 / –0.413	0.725 / –0.320

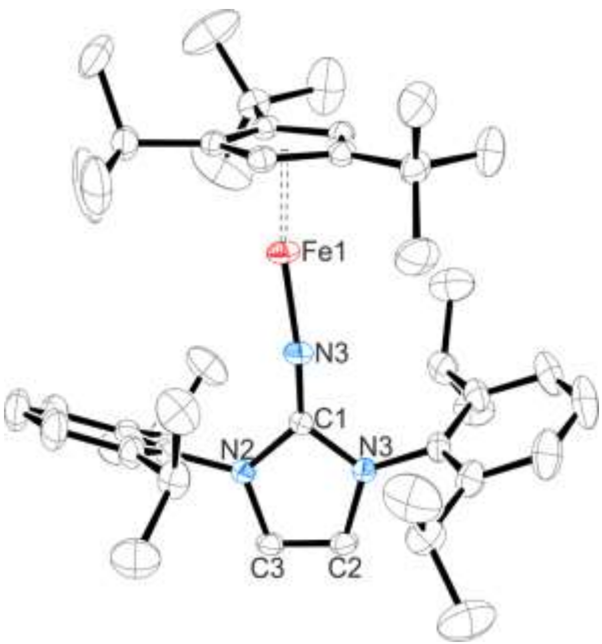

Figure S9. ORTEP diagram of complex **2-Fe** with thermal displacement parameters drawn at the 30 % probability levels at a temperature of 250 K. Hydrogen atoms are omitted for clarity. Selected bond lengths [Å] and angles [°]: Fe–N3 1.7793(13), N3–C1 1.2538(18), Cp‘$_{cent}$–Fe 1.90, Cp‘$_{cent}$–Fe–N3 168.59, Fe–N3–C1 173.15(11), N1–C1–N2 103.00(13).

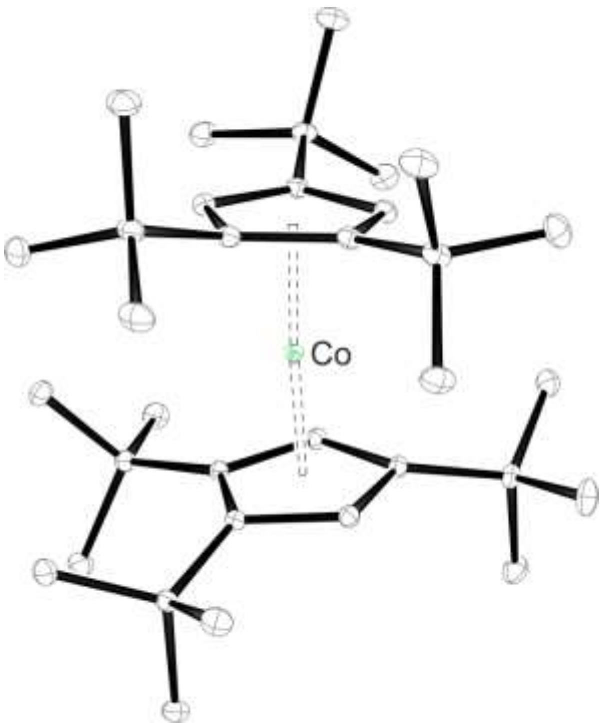

Figure S10. ORTEP diagram of one of the two molecules of the asymmetric unit of complex [Cp’$_2$Co] with thermal displacement parameters drawn at the 50 % probability levels. Hydrogen atoms are omitted for clarity. The metric parameters of the second molecule in the asymmetric unit are provided in parenthesis. Selected bond lengths [Å] and angles [°] of molecule 1 (molecule 2): Cp’$_{cent1}$–Co 1.79 (1.80), Cp’$_{cent2}$–Co 1.80 (1.80), Cp‘$_{cent1}$–Co–Cp‘$_{cent2}$ 174.51 (174.75).

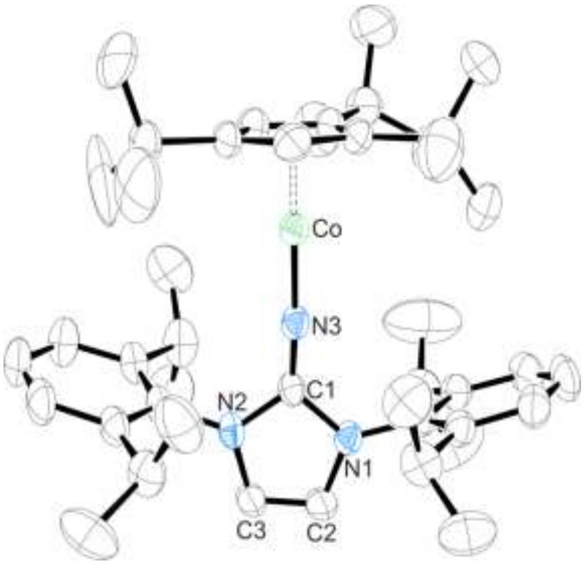

Figure S11. ORTEP diagram of one of the two molecules in the asymmetric unit of complex **2-Co** with thermal displacement parameters drawn at the 30 % probability levels at a temperature of 273 K. Hydrogen atoms are omitted for clarity. Selected bond lengths [Å] and angles [°] of molecule 1 (molecule 2): Co–N3 1.721(4) (1.725(4)), Cp‘$_{cent}$–Co 1.723(2) (1.721(2)), C1–N3 1.263(5) (1.259(5)), Cp‘$_{cent}$–Co–N 177.27(15) (179.37(15)), Co–N3–C1 173.1(3) (176.3(3)), N1–C1–N2 102.3(3) (103.0(4)).

Figure S12. Crystal of **2-Co** at a temperature of 100 K.

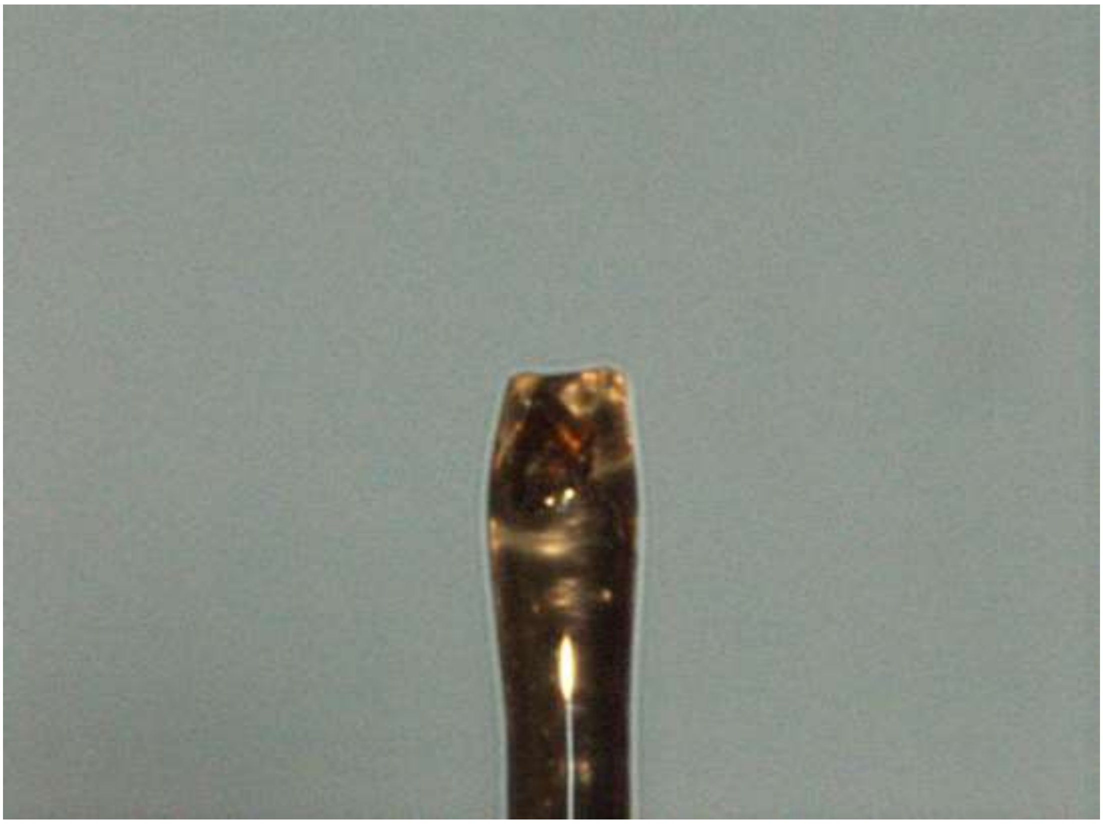

Figure S13. Crystal of **2-Co** at a temperature of 273 K.

S4 Solid-state magnetic susceptibility

General considerations. Solid-state magnetic susceptibility measurements were performed on a Cryogenic Ltd. closed-cycle SQUID magnetometer between T = 2.6 and 300 K with an externally applied magnetic field of H_{ext} = 1 kOe. The samples were prepared in quartz tubes as previously described.[9] The diamagnetic background signal of an empty sample holder including quartz wool was experimentally determined and subtracted from the raw magnetization data. The experimental data were also corrected for the overall diamagnetism of the investigated molecules by using an approximation, given by $\chi_D = -M_w/2\ \times 10^{-6}$ emu g^{-1} where M_w denotes the molecular weight of the substance.[10] To ensure the validity of the Curie-law approximation for an applied magnetic field of H_{ext} = 1 kOe used in the temperature-dependent measurements mentioned above, supplementary measurements at T = 2.6 K with applied magnetic fields between H_{ext} = 1 and 10 kOe were executed.

Addenda magnetization measurements. Isothermal magnetization measurements at temperatures between T = 4 and 23 K with externally applied magnetic fields between H_{ext} = 0.25 and 50 kOe were conducted on **2-Fe** (cf., Figures S16 and S17) and **3-Co** (cf., Figures S22 and S23), respectively. Furthermore, auxiliary variable temperature and variable field (VTVH) magnetization measurements at temperatures between T = 4 and 100 K with externally applied magnetic fields of H_{ext} = 10, 30 and 50 kOe were also executed on **3-Co** (cf., Figure S21).

As already discussed in the main text**,** the fit result on the VTVH magnetization data of **3-Co** strongly depends on the starting values of the fit parameters. Hence, we also analyzed the VTVH measurements by systematic variation of a fixed rhombic ZFS parameter *E/D* (cf., Tables S3 and S4), assuming two restricted models with (1) an axial g-tensor anisotropy with $g_1 = g_2 < g_3$ and (2) a fixed g-value anisotropy with g_1 = 1.37, g_2 = 1.85 and g_3 = 3.58 as determined by the temperature-dependent magnetic susceptibility measurements. While the first ansatz revealed an *E/D* value of approximately zero, the second ansatz confirmed the large *E/D* value (i.e., $E/D \approx 0.28$) that was also extracted from the analysis of our temperature-dependent magnetic susceptibility measurements. These contradicting results obtained for the two models (1) and (2) might be artificially introduced by the different restrictions applied.

Alternatively, the isothermal magnetization measurements on **3-Co** were analyzed by a combined fit assuming an effective g-value, which enabled us to simulate different *D* values in the range between *D* = +100 and -100 cm^{-1} (cf., Figure S24). However, this analysis again revealed a rhombic ZFS parameter of *E/D* = 0, presumably caused by the restrictions used in this model. Therefore, this sensitivity analysis only confirms the value of the determined magnitude – and not the sign – of the axial ZFS parameter *D* exerted by our magnetic susceptibility, VTVH and X-band EPR measurements described in the main text.

Table S2. Summary of fit parameters obtained by a Curie-Weiss fit of the inverse magnetic susceptibility data (cf., Figure S14, S19 and S27), where μ_C describes the corresponding effective magnetic moment, while χ_{TIP} denotes a phenomenological temperature-independent contribution to the magnetic susceptibility.

	C (cm^3 mol^{-1} K)	θ (K)	χ_{TIP} (10^{-4} cm^3 mol^{-1})	μ_C (μ_B)	μ_{eff} (μ_B)
2-Fe	3.897(3)	-4.6(1)	-	5.58	5.52 [c]
3-Co	3.70(1)	-3.0(2)	-13(1) [b]	5.44	5.13 [c]
2-Co [a]	0.444(1)	-0.79(4)	6.04(9)	1.88	1.92 [d]

[a] Fit below T = 120 K. [b] The large negative TIP value reflects the declining effective magnetic moment that is observed above approx. T = 130 K (cf., Figure S18) and attributed to g-value anisotropy (see main text). [c] At T = 300 K. [d] At T = 40 K.

Table S3. Summary of fit parameters obtained from a combined analysis of the VTVH magnetization measurements on **3-Co** by systematically variation of a fixed rhombic ZFS parameter *E/D* and by assuming an axial g-tensor anisotropy with $g_1 = g_2 < g_3$. *R* describes the corresponding quality of the fit with *julX*.[11]

E/D	*D* (cm^{-1})	$g_1 = g_2$	g_3	*R* (10^{-5})
0.03*	-124.2	1.95	3.40	0.808
0.08*	-122.2	1.94	3.41	0.928
0.13*	-117.8	1.90	3.43	1.18
0.18*	-116.5	1.84	3.47	1.67
0.23*	-112.9	1.77	3.51	2.16
0.28*	-108.9	1.65	3.57	2.58
0.33*	-88.7	0.98	3.70	8.99

* Fixed in the fit.

Table S4. Summary of the parameters obtained from a combined analysis of the VTVH magnetization measurements on **3-Co** by a systematically variation of a fixed rhombic ZFS parameter *E/D* and by assuming a fixed g-value anisotropy with $g_1 = 1.37$, $g_2 = 1.85$ and $g_3 = 3.58$, determined by our temperature-dependent magnetic susceptibility measurements. *R* describes the corresponding quality of the fit with *julX*.[11]

E/D	*D* (cm^{-1})	g_1	g_2	g_3	*R* (10^{-4})
0.03*	**	1.37*	1.85*	3.58*	37.0
0.08*	**	1.37*	1.85*	3.58*	28.3
0.13*	**	1. 37*	1.85*	3.58*	16.1
0.18*	**	1. 37*	1.85*	3.58*	7.24
0.23*	-202.5	1. 37*	1.85*	3.58*	2.10
0.28*	-96.5	1. 37*	1.85*	3.58*	0.304
0.33*	-50.8	1. 37*	1.85*	3.58*	2.17

* Fixed in the fit. ** Not a number.

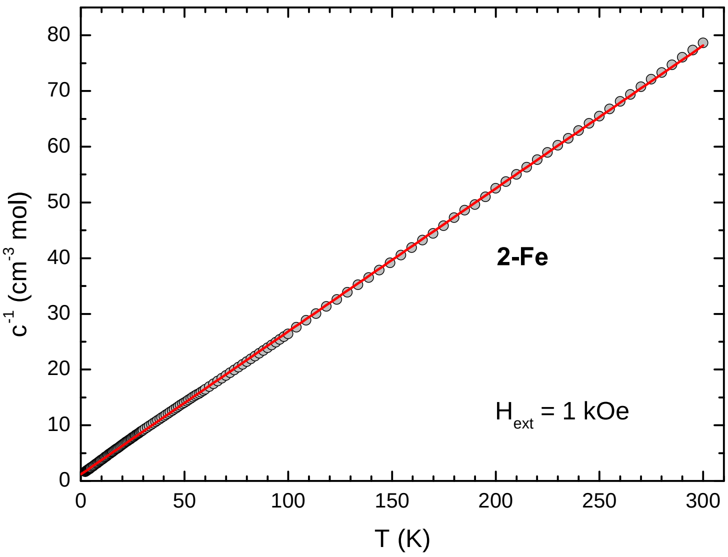

Figure S14. Inverse magnetic susceptibility (χ^{-1}) vs. T plot for **2-Fe** recorded between T = 3 and 300 K with an externally applied magnetic field of H_{ext} = 1 kOe. Symbols: Experimental data. Line: Fit with a Curie-Weiss model. The parameters of the fit are summarized in Table S2.

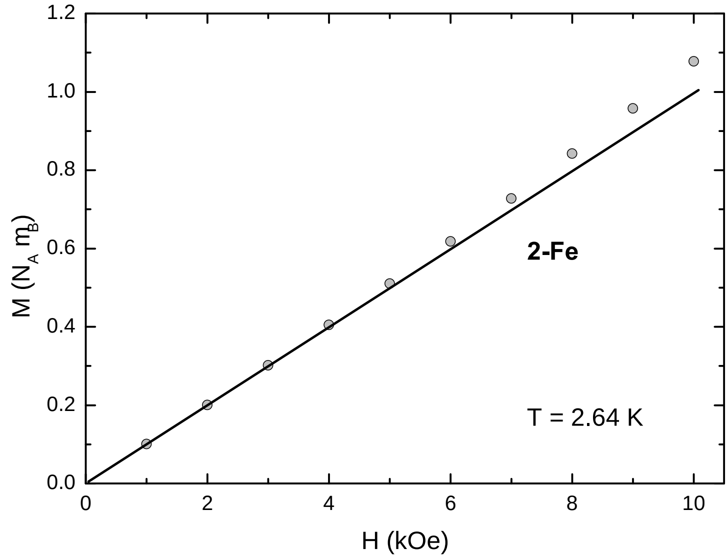

Figure S15. Isothermal magnetization (M) vs. magnetic field (H) plot for **2-Fe** recorded at T = 2.64 K with externally applied magnetic fields between H_{ext} = 1 and 10 kOe. Symbols: Experimental data. The line represents the linear M(H) progression as expected in the Curie-Weiss approximation.

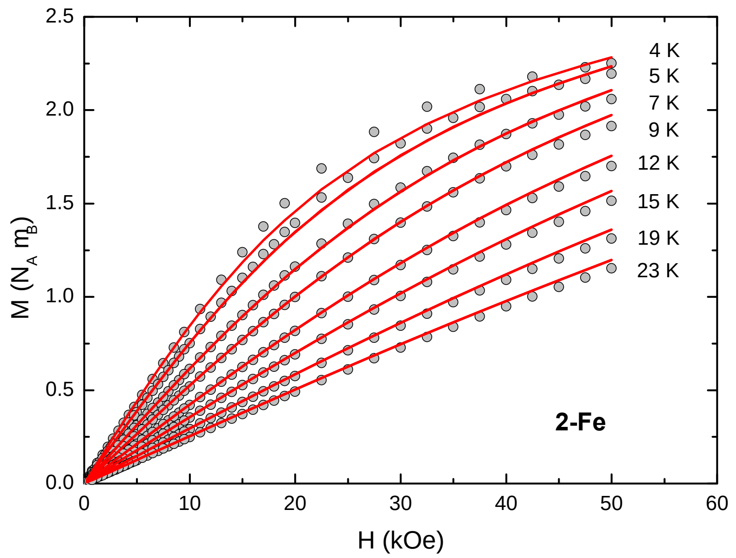

Figure S16. Isothermal magnetization (M) vs. magnetic field (H) plot for **2-Fe** recorded at temperatures between T = 4 and 23 K with externally applied magnetic fields between H_{ext} = 0.25 and 50 kOe. Symbols: Experimental data. Lines: Combined fit based on a spin-Hamiltonian approach (parameters of the fit: g_{eff} = 2.31, D = -20.5 cm^{-1} and E/D = 0.32).

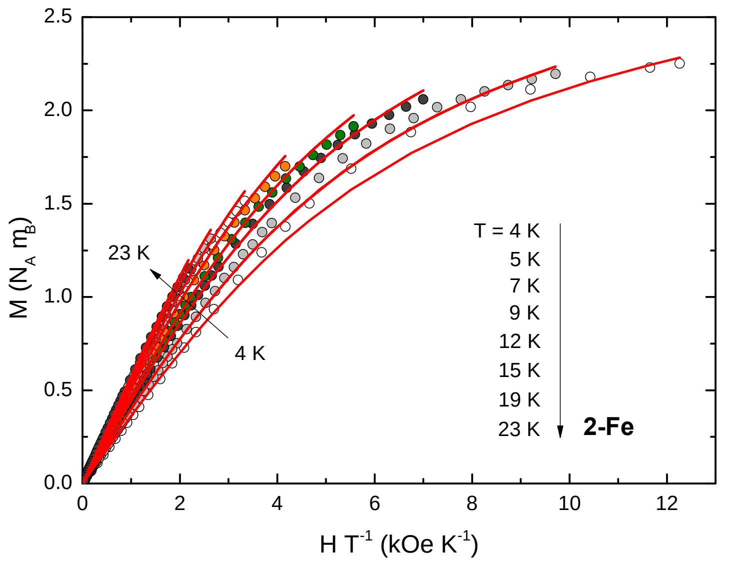

Figure S17. Isothermal magnetization (M) vs. magnetic field (H/T) plot for **2-Fe** recorded at temperatures between T = 4 and 23 K with externally applied magnetic fields between H_{ext} = 0.25 and 50 kOe. Symbols: Experimental data (i.e., the same data as also shown in Figure S16). Lines: Combined fit based on a spin-Hamiltonian approach (parameters of the fit: g_{eff} = 2.31, D = -20.5 cm^{-1} and E/D = 0.32).

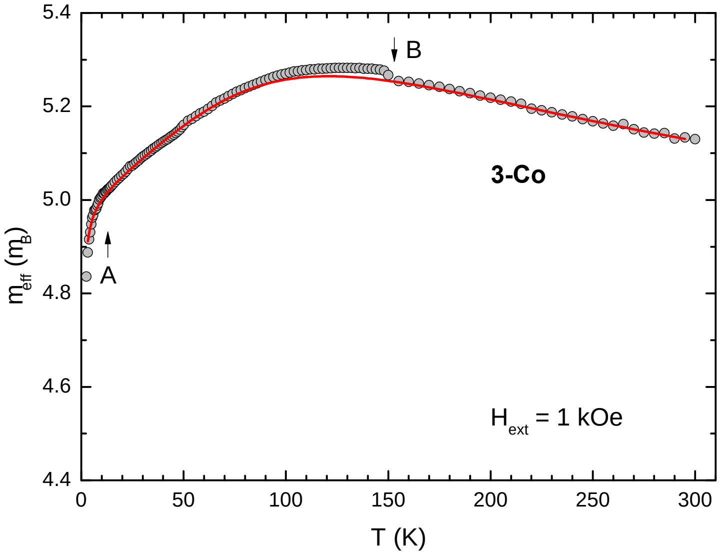

Figure S18. Effective magnetic moment (μ_{eff}) vs. T plot for **3-Co** recorded between T = 3 and 300 K with an externally applied magnetic field of H_{ext} = 1 kOe. Symbols: Experimental data. Line: Fit based on a spin-Hamiltonian approach by systematic variation of the *E/D* values between 0 and 0.33. The line represents the best fit that was achieved with parameters: g_1 = 1.37, g_2 = 1.85, g_3 = 3.58, *D* = -101.7 cm^{-1} and (fixed) *E/D* = 0.33. Labels in the diagram: (A) To account for the experimental data at low temperatures, we also considered weak antiferromagnetic (intermolecular) coupling of *J* = -0.4 cm^{-1} (fixed in the fit) between the magnetic moments of surrounding molecules. (B) This step in the effective magnetic moment may be associated with a structural phase transition in **3-Co** occurring at approx. T = 150 K.

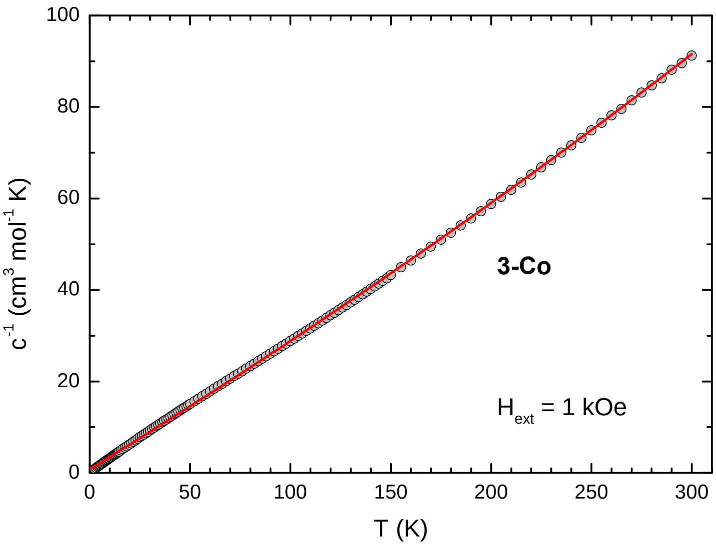

Figure S19. Inverse magnetic susceptibility (χ^{-1}) vs T plot for **3-Co** recorded between T = 3 and 300 K with an externally applied magnetic field of H_{ext} = 1 kOe. Symbols: Experimental data. Line: Fit with a Curie-Weiss model. The parameters of the fit are summarized in Table S2.

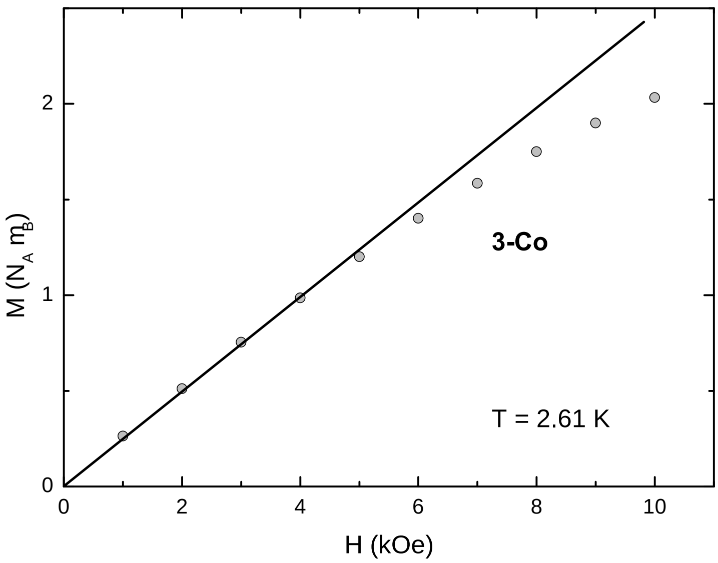

Figure S20. Isothermal magnetization (M) vs. magnetic field (H) plot for **3-Co** recorded at T = 2.61 K with externally applied magnetic fields between H_{ext} = 1 and 10 kOe. Symbols: Experimental data. The line represents the linear M(H) progression as expected in the Curie-Weiss approximation.

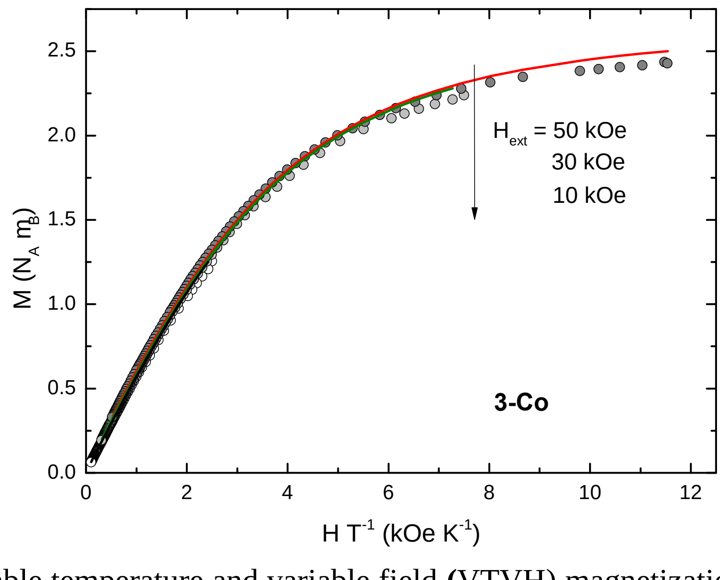

Figure S21. Variable temperature and variable field **(**VTVH) magnetization (M) vs. magnetic field (H/T) plot for **3-Co** recorded at temperatures between T = 4 and 100 K with externally applied magnetic fields of H_{ext} = 10, 30 and 50 kOe. Symbols: Experimental data. Lines: Combined fit based on a spin-Hamiltonian approach (parameters of the fit: g_1 = 1.42, g_2 = 1.95, g_3 = 3.58, D = -99.7 cm^{-1} and E/D = 0.29).

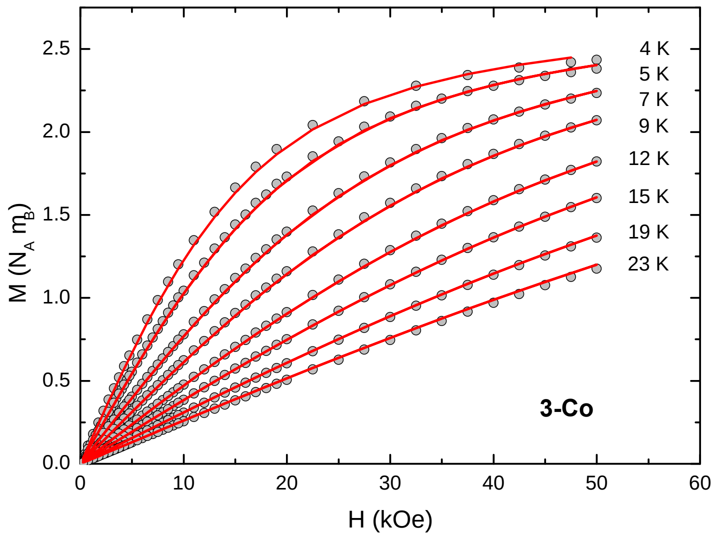

Figure S22. Isothermal magnetization (M) vs. magnetic field (H) plot for **3-Co** recorded at temperatures between T = 4 and 23 K with externally applied magnetic fields between H_{ext} = 0.25 and 50 kOe. Symbols: Experimental data. Lines: Combined fit based on a spin-Hamiltonian approach (parameters of the fit: g_{eff} = 3.29, (fixed) D = -100 cm^{-1} and E/D = 0, see text for details).

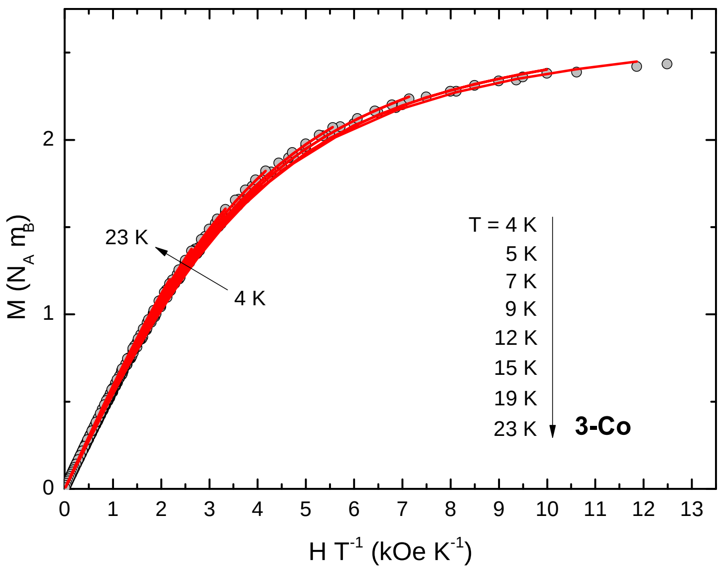

Figure S23. Isothermal magnetization (M) vs. magnetic field (H/T) plot for **3-Co** recorded at temperatures between T = 4 and 23 K with externally applied magnetic fields between H_{ext} = 0.25 and 50 kOe. Symbols: Experimental data (i.e., the same data as also shown in Figure S22). Lines: Combined fit based on a spin-Hamiltonian approach (parameters of the fit: g_{eff} = 3.29, (fixed) D = -100 cm^{-1} and E/D = 0, see text for details).

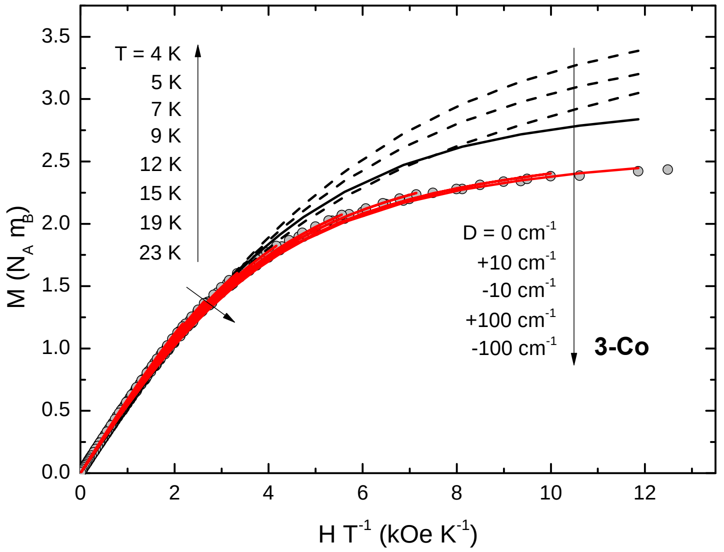

Figure S24. Isothermal magnetization (M) vs. magnetic field (H/T) plot for **3-Co** recorded at temperatures between T = 4 and 23 K with externally applied magnetic fields between H_{ext} = 0.25 and 50 kOe. Symbols: Experimental data (i.e., the same data as also shown in Figures S22 and S23). Red lines: Combined fit based on a spin-Hamiltonian approach (parameters of the fit: g_{eff} = 3.29, (fixed) D = -100 cm^{-1} and E/D = 0, see text for details). Black lines: Fit of the data recorded at T = 4 K based on a spin-Hamiltonian approach with different (fixed) D-values of D = -100, -10, 0, 10 and 100 cm^{-1} but variable g_{eff} and E/D.

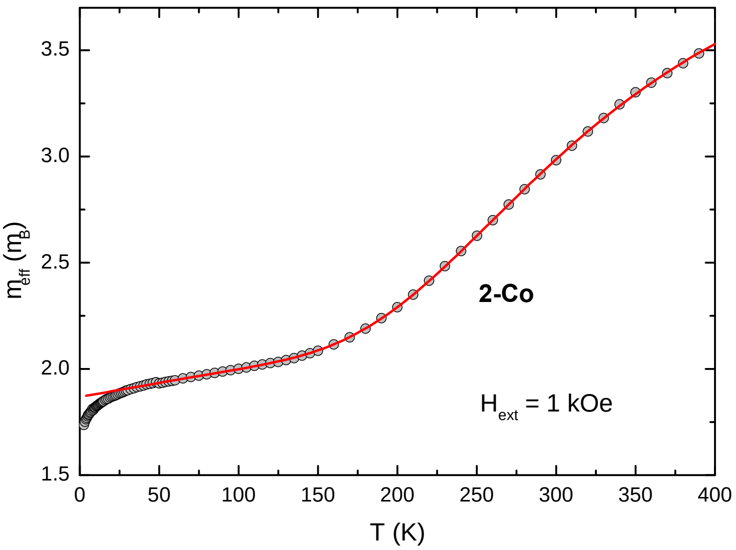

Figure S25. Effective magnetic moment (μ_{eff}) vs T plot for **2-Co** recorded between T = 3 and 390 K with an externally applied magnetic field of H_{ext} = 1 kOe. Symbols: Experimental data. Line: Fit (for T > 50 K) with a modified regular solution model described in the main text (parameters of the fit: μ_{LS} = 1.868(2) μ_B, μ_{HS} = 4.42(3) μ_B, ΔH = 9714(92) J mol^{-1}, ΔS = 24.1(5) J mol^{-1} K^{-1}, and χ_{TIP} = 6.25(10) $\cdot$ 10^{-4} cm^3 mol^{-1}).

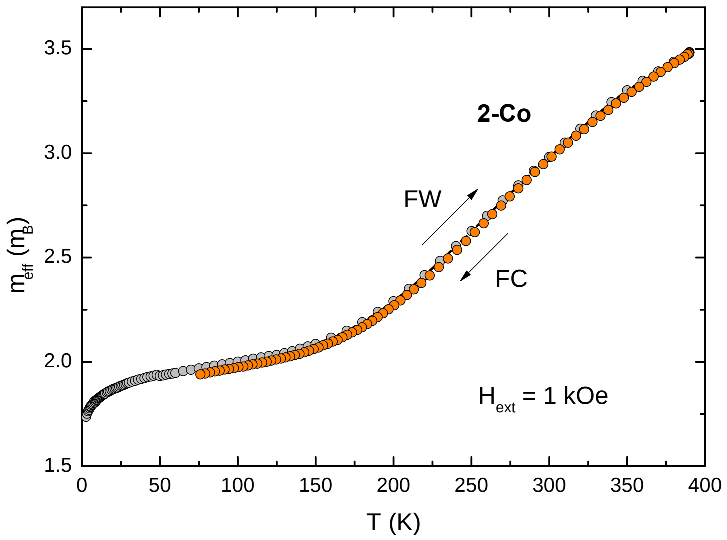

Figure S26. Effective magnetic moment (μ_{eff}) vs. T plot for **2-Co** recorded between T = 3 and 390 K with an externally applied magnetic field of H_{ext} = 1 kOe. Symbols plotted in grey: Experimental data recorded with a standard field-warming (FW) sequence after zero-field cooling. Symbols plotted in orange: Experimental data recorded under field-cooling (FC) conditions with an externally applied magnetic field of H_{ext} = 1 kOe and a constantly decreasing temperature (ramp rate of approx. 0.4 K/min). Marginal deviations between both measurements are attributed to a small temperature gradient or drift at the sample site that is inherent for measurements with constantly changing temperatures.

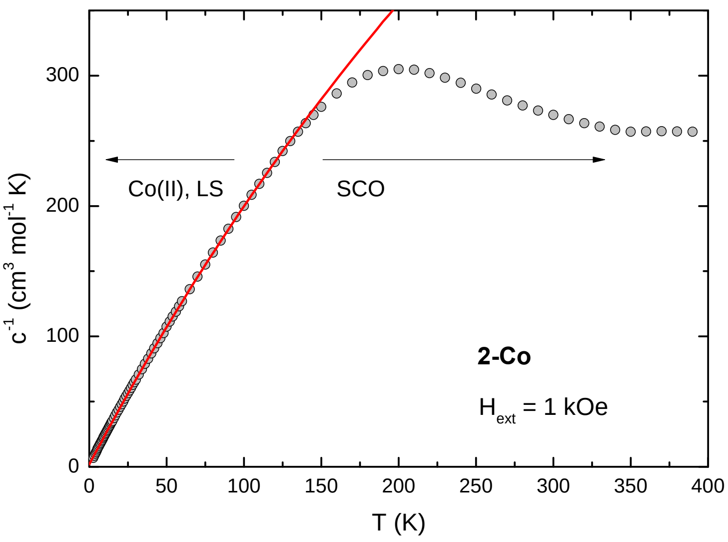

Figure S27. Inverse magnetic susceptibility (χ^{-1}) vs. T plot for **2-Co** recorded between T = 3 and 390 K with an externally applied magnetic field of H_{ext} = 1 kOe. Symbols: Experimental data. Line: Fit with a Curie-Weiss model described in the main text. The parameters of the fit are summarized in Table S2. The label "SCO" denotes the onset of the spin-crossover.

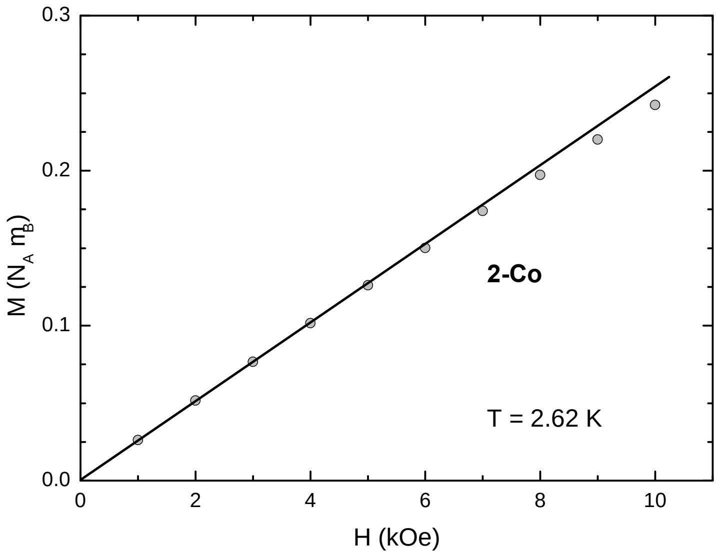

Figure S28. Isothermal magnetization (M) vs. magnetic field (H) plot for **2-Co** recorded at T = 2.62 K with externally applied magnetic fields between H_{ext} = 1 and 10 kOe. Symbols: Experimental data. The line represents the linear M(H) progression as expected in the Curie-Weiss approximation.

S5 X-band EPR spectroscopy

X-band EPR spectra were recorded on a Bruker EMX spectrometer with an OXFORD ESR900 continuous flow cryostat at the given temperatures. Solutions of the cobalt complexes **2-Co** and **3-Co**, respectively, were prepared in quartz tubes (707-SQ-250M, Wilmad-LabGlass). The spectra were simulated with EasySpin 5.2.25.[12]

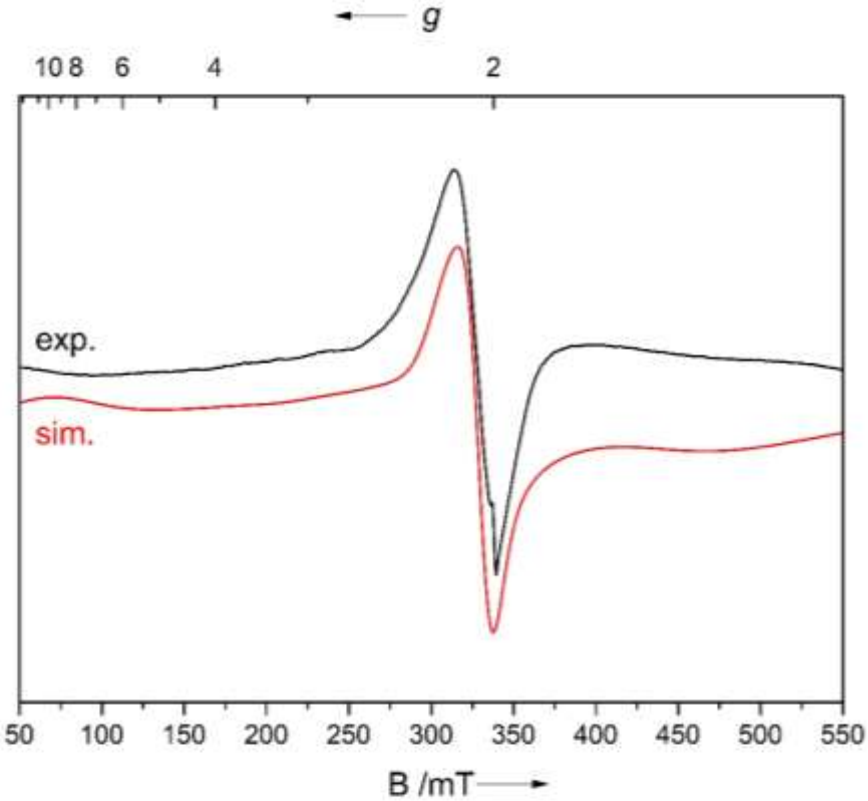

Figure S29. X-band EPR spectrum (black) and simulation (red) for complex **3-Co** measured in toluene (T = 12.0 K, ν = 9.45938 GHz). The simulation was executed assuming an $S = 3/2$ spin state and fixed zero-field splitting parameters of $D = -100\ cm^{-1}$ and $E/D = 0.33$ as suggested by our solid-state magnetic susceptibility measurements on **3-Co** (cf., main text and Figure S18). The determined g-values are: $g_1 = 1.58$, $g_2 = 2.05$, $g_3 = 3.67$ with g_{strain} = [0.250; 0.081; 3.44] as line broadening parameters. Large line broadening parameters are often observed for Co(II) high-spin complexes, indicating the presence of sample inhomogeneities as well as unresolved ^{59}Co hyperfine coupling.[13,14]

S6 Zero-field ^{57}Fe Mössbauer spectroscopy

General considerations. Zero-field ^{57}Fe Mössbauer measurements were performed on a standard transmission spectrometer with sinusoidal velocity sweep. Velocities were calibrated using an α-Fe foil at ambient temperature and confirmed by measurements with powders of sodium nitroprusside or potassium ferrocyanide. Polycrystalline powders of complex **2-Fe** were prepared with an area density corresponding to *ca.* 0.10 mg ^{57}Fe/cm^2 and were filled in sample containers made of Teflon or PEEK (polyether ether ketone). The temperature-dependent measurements were executed on a CryoVac continuous-flow cryostat with helium exchange gas (adjusted at approximately 50-100 mbar). The temperature was recorded with a calibrated Si diode located close to the sample container, indicating a temperature stability of better than 0.1 K. The minimum experimental line width (HWHM) was < 0.12 mm s^{-1}. The Mössbauer source, with nominal activity of about 50 mCi of ^{57}Co in a rhodium matrix, was stored at ambient temperature during the measurement. Isomer shifts (δ) are quoted relative to metallic iron at room temperature but were not corrected in terms of the second-order Doppler shift. The Mössbauer spectra were analyzed with the longitudinal relaxation model developed by Blume and Tjon[15] utilizing *Recoil*[16] and *Mathematica*.[17]

Within the Blume-Tjon relaxation model and in case of intermediate spin-spin and spin-lattice relaxation, the local hyperfine magnetic field (H_{hf}) and the fluctuation rate (ν_c) of this field at the ^{57}Fe nucleus site are strongly correlated with each other and cannot simultaneously be determined.[15] Because the local hyperfine magnetic field in **2-Fe** is not known, we estimated $\mathrm{H_{hf}}$ by use of the "110 kOe per unpaired spin" rule which is a good approximation for the Fermi contact contribution (H_{FC}).[18] Usually, the dipolar and orbital contributions (H_{D} and H_{O}, respectively) are small and the Fermi contact field provides the main contribution to H_{hf}. However, the orbital contributions can also be large when an unquenched electronic orbital angular momentum is present; but on basis of the available data an estimate of H_O would be very speculative for **2-Fe**. Hence, we only used the Fermi contact field in our simulations and, thus, within the analysis presented here (cf., Table S5), only the ratio $\nu_c/\mathrm{H_{hf}}$ has a physical meaning and not the individual values of ν_c and H_{hf}.

Beside these limitations, the simulations of the Mössbauer spectra (with a single Fe site and a small impurity fraction of *ca.* 6%) are in good agreement with the experimental data recorded at T = 100 and 200 K (cf., Figures 2 and S30). However, for the spectrum measured at T = 20 K significant deviations between theory and experiment are obvious. This can be attributed to zero-field splitting and the thermal population of the respective $m_s = \pm2, \pm1$ and 0 states. Generally, every m_s-state is associated with an individual local magnetic hyperfine field and relaxation time and, therefore, the Mössbauer spectrum consists in this case of three individual hyperfine spectra.[18,19] While a fit with three iron sites was not possible in the present case (i.e., due to strong correlations between the large number of parameters that are associated with this model), we obtained a good result with two components (cf., Figure S31). With this rough approximation and assuming simple Boltzmann statistics, we further estimated (an upper limit) for the axial ZFS parameter of approx. $D < -6$ cm^{-1} that agrees fairly well with the $|D|$ value of approx. 20 cm^{-1} and $D = -20.5$ cm^{-1} determined by our solid-state magnetic susceptibility and isothermal magnetization measurements, respectively (*vide supra*).

Table S5. Mössbauer parameters of **2-Fe** obtained from the fits described in the text. Isomer shifts (δ) are specified relative to metallic iron at room temperature and were not corrected in terms of the second order Doppler shift. The quadrupole splitting is given by $\Delta E_Q = 2\,\varepsilon$ with $\varepsilon = e^2 q\, Q/4$ and $\eta = 0$ (with e, q, Q, and η used in their usual meaning).

T (K)	δ (mm s^{-1})	ε (mm s^{-1})	Γ_{HWHM} (mm s^{-1})	H_{hf} (kOe)	ν_C (mm s^{-1})	V (%)
200	0.782(11)	0.247(11)	0.206(9)	440*	229(29)	93.0
	0.38(7)	0.67(8)	0.206(8)	-**	-	7.0
100	0.867(8)	0.341(7)	0.233(9)	440*	109(6)	94.3
	0.55(4)	0.56(4)	0.21*	-**	-	5.7
20	0.957(12)	0.457(11)	0.376(11)	440*	46(3)	94.9
	0.55*	0.56*	0.21*	-**	-	5.1
20 [a]	0.83(8)	0.11(9)	0.23*	440*	7(1)	65.7
	0.936(12)	0.518(9)	0.23*	440*	117(16)	29.7
	0.55*	0.56*	0.21*	-**	-	4.5

* Fixed in the fit; ** Fit with a doublet of Lorentzian lines (i.e. the fast (dynamic) limit within the framework of the Blume-Tjon relaxation model); [a] Alternative fit assuming two iron sites for the main signal (beside an impurity fraction of about 6 %).

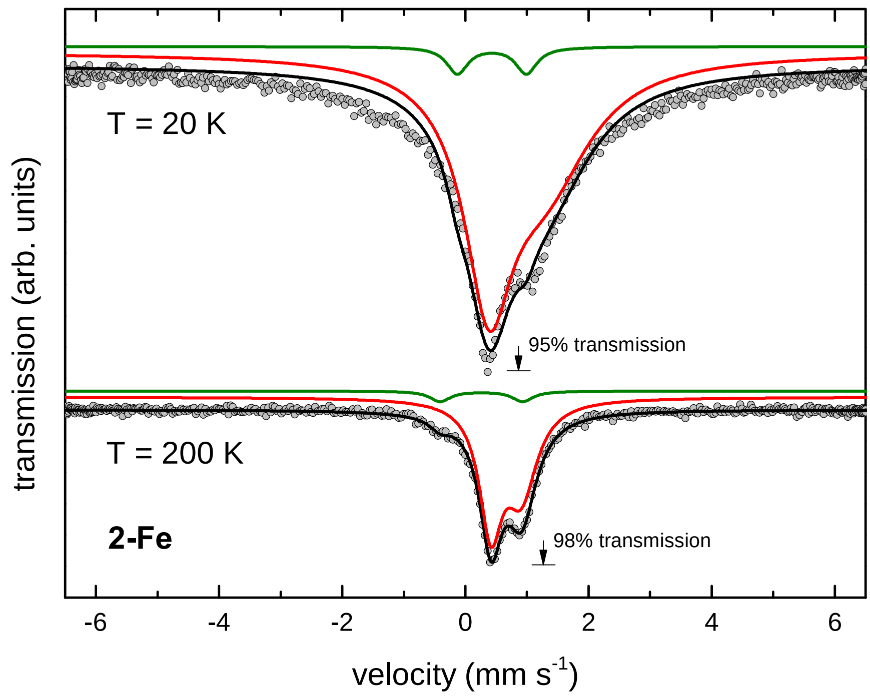

Figure S30. Zero-field Mössbauer spectra for **2-Fe** recorded at T = 20 and 200 K. Symbols: Experimental data. Red line: Fit based on the Blume-Tjon relaxation model as described in the text; the line plotted in green is associated with a small but unidentified impurity of ca. 6 % volume fraction that might be introduced during the sample handling prior to the measurements. The black line represents the superposition of both contributions. The parameters of the fit are summarized in Table S5.

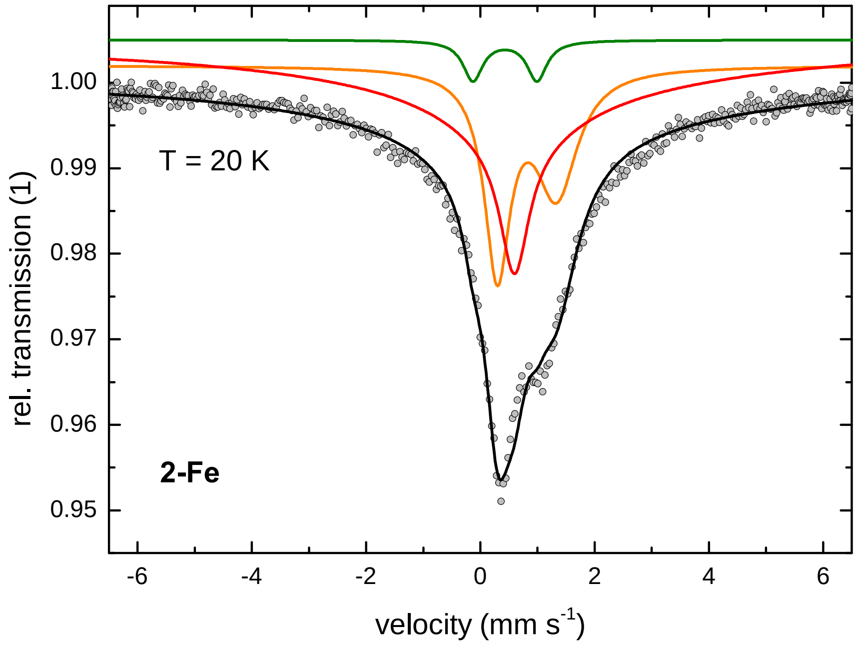

Figure S31. Zero-field Mössbauer spectra for **2-Fe** recorded at T = 20 K. Symbols: Experimental data. Red and orange line: Two-component fit based on the Blume-Tjon relaxation model as described in the text; the line plotted in green is associated with a small but unidentified impurity of ca. 6 % volume fraction that might be introduced during the sample handling prior to the measurements. The black line represents the superposition of these three components. The parameters of the fit are summarized in Table S5.

S7 Cyclovoltammetry

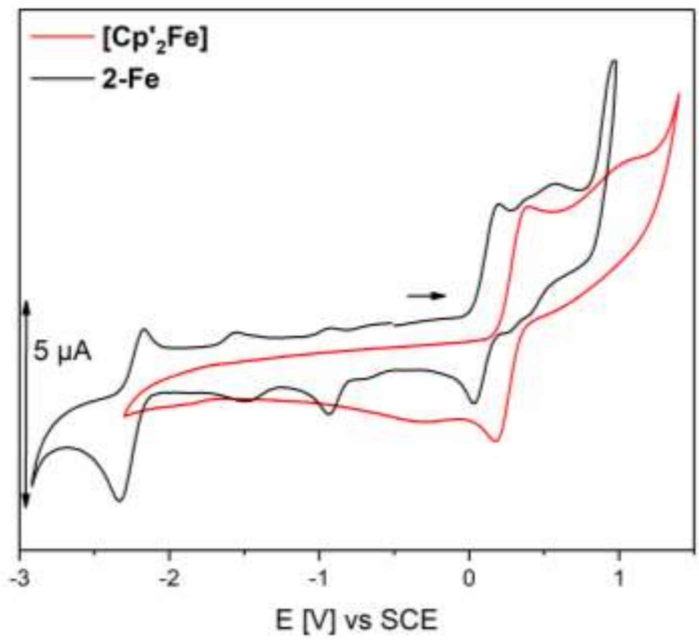

Figure S32. Cyclic voltammograms for **2-Fe** and [Cp'$_2$Fe], recorded at ambient temperature in THF with 0.1 M [*n*-Bu$_4$N][PF$_6$] supporting electrolyte at a scan rate of 100 mV/s: **2-Fe**: $E_{1/2,\ ox}$ = 0.115 V, $E_{1/2,\ red}$ = –2.252 V; [Cp'$_2$Fe]: $E_{1/2,\ ox}$ = 0.285 V.

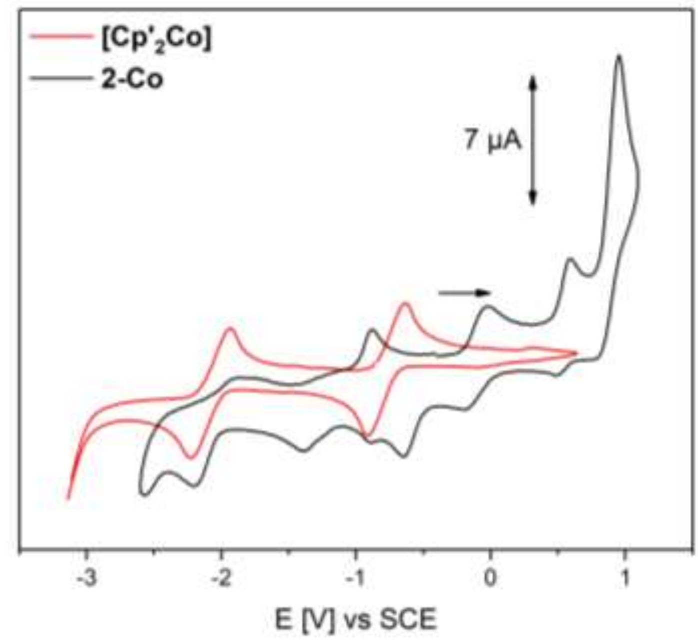

Figure S33. Cyclic voltammograms for **2-Co** and [Cp'$_2$Co], recorded at ambient temperatures in THF with 0.1 M [*n*-Bu$_4$N][PF$_6$] supporting electrolyte at a scan rate of 100 mV s^{-1}: [Cp'$_2$Co]: $E_{1/2,\ ox}$ = –0.774 V; $E_{1/2,\ red}$ = –2.081 V.

S8 UV/Vis spectroscopy

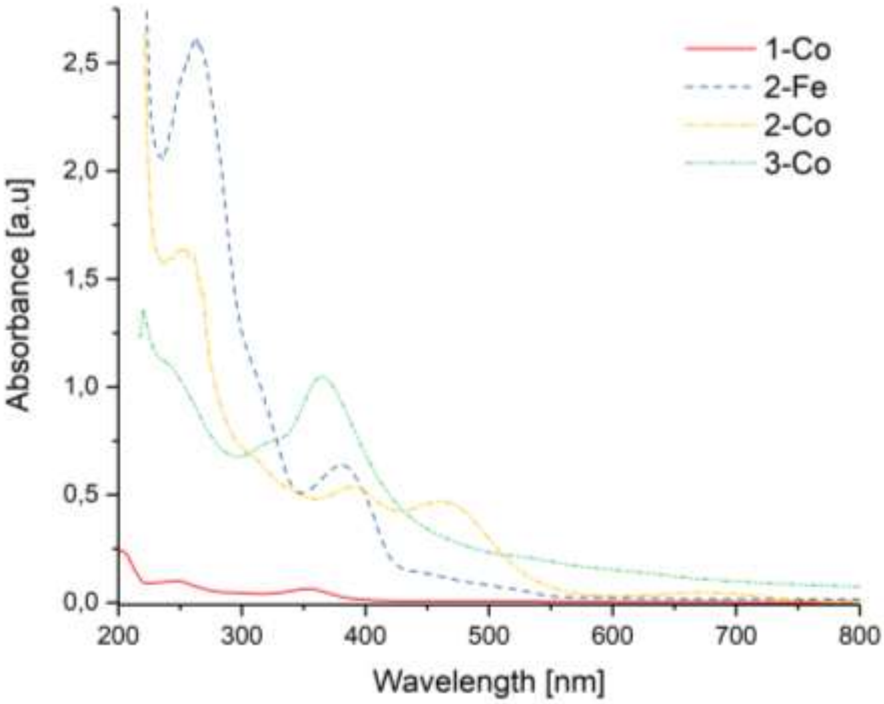

Figure S34. UV/Vis spectra for **1-Co**, **2-M** (M = Fe, Co) and **3-Co** recorded in *n*-hexane at 25 °C.

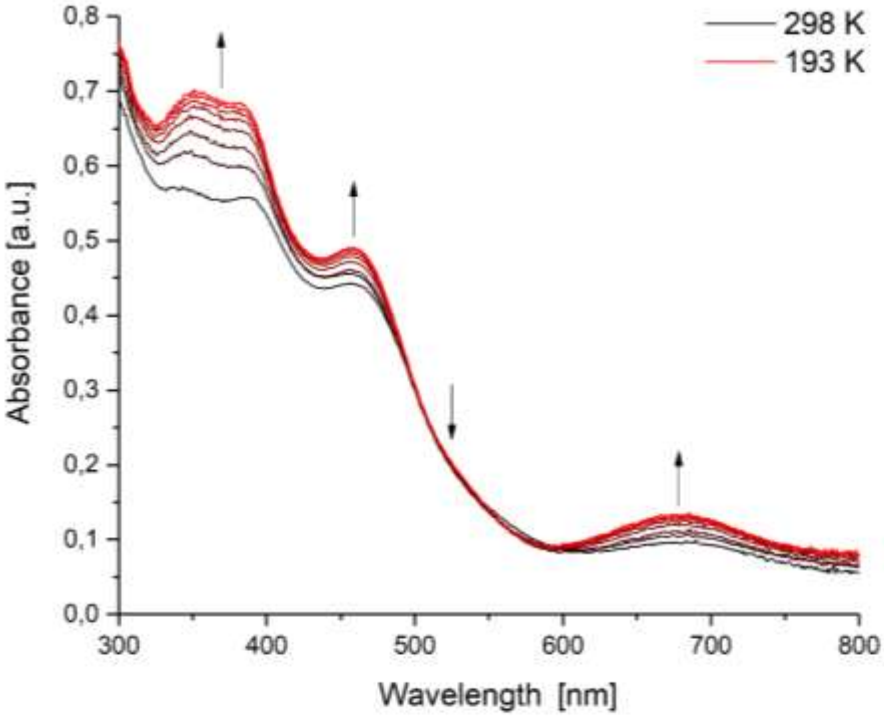

Figure S35. Variable temperature UV/Vis spectra for **2-Co** recorded in *n*-hexane.

S9 Computational studies

All calculations employed the B3LYP[20] functional and were carried out with Gaussian 09.[21] No symmetry restrictions were imposed (C1). C, H, N, Fe and Co were represented by an all-electron 6-311G(d,p) basis set. The nature of extrema (minima) was established with analytical frequencies calculations. The zero-point vibration energy (ZPE) and entropic contributions were estimated within the harmonic potential approximation. Geometrical parameters were reported within an accuracy of 10^{-3} Å and 10^{-1} degrees.

Table S6. Energies of the optimized structures

Compound	E(0 K)[b] [Ha]	H(298 K)[c] [Ha]	G(298 K)[c] [Ha]
[Cp'Fe(NIm^{Dipp})] (S=0)	-3143.263781 (22.1)	-3143.208757 (21.4)	-3143.351649 (25.4)
[Cp'Fe(NIm^{Dipp})] (S=1)	-3143.250119 (30.7)	-3143.194710 (30.2)	-3143.338439 (33.7)
[Cp'Fe(NIm^{Dipp})] (S=2)	-3143.299053 (0.0)	-3143.242892 (0.0)	-3143.392143 (0.0)
[Cp'Co(NIm^{Dipp})] (S=1/2)	-3262.330699 (0.0)	-3262.275418 (0.0)	-3262.418544 (0.0)
[Cp'Co(NIm^{Dipp})] (S=3/2)	-3262.324588 (3.8)	-3262.268719 (4.2)	-3262.415160 (2.1)

[a]Values (in kcal/mol) given in parenthesis refer to the energy difference to the lowest computed spin-configuration for the individual compounds. [b]DFT energy incl. ZPE. [c]Standard conditions T = 298.15 K and p = 1 atm.

Löwdin and Mulliken reduced orbital charges and spin populations for compound **2-Fe** were computed with the ORCA program package.[22]

Table S7. Löwdin and Mulliken reduced orbital charges and spin populations for **2-Fe**

d-orbital	Löwdin	Mulliken
d_{z2}	1.361286	1.342169
d_{xz}	1.376572	1.355121
d_{yz}	1.307019	1.280308
$d_{x^2-y^2}$	1.243116	1.208557
d_{xy}	1.166815	1.138065
d total:	6.454808	6.324220

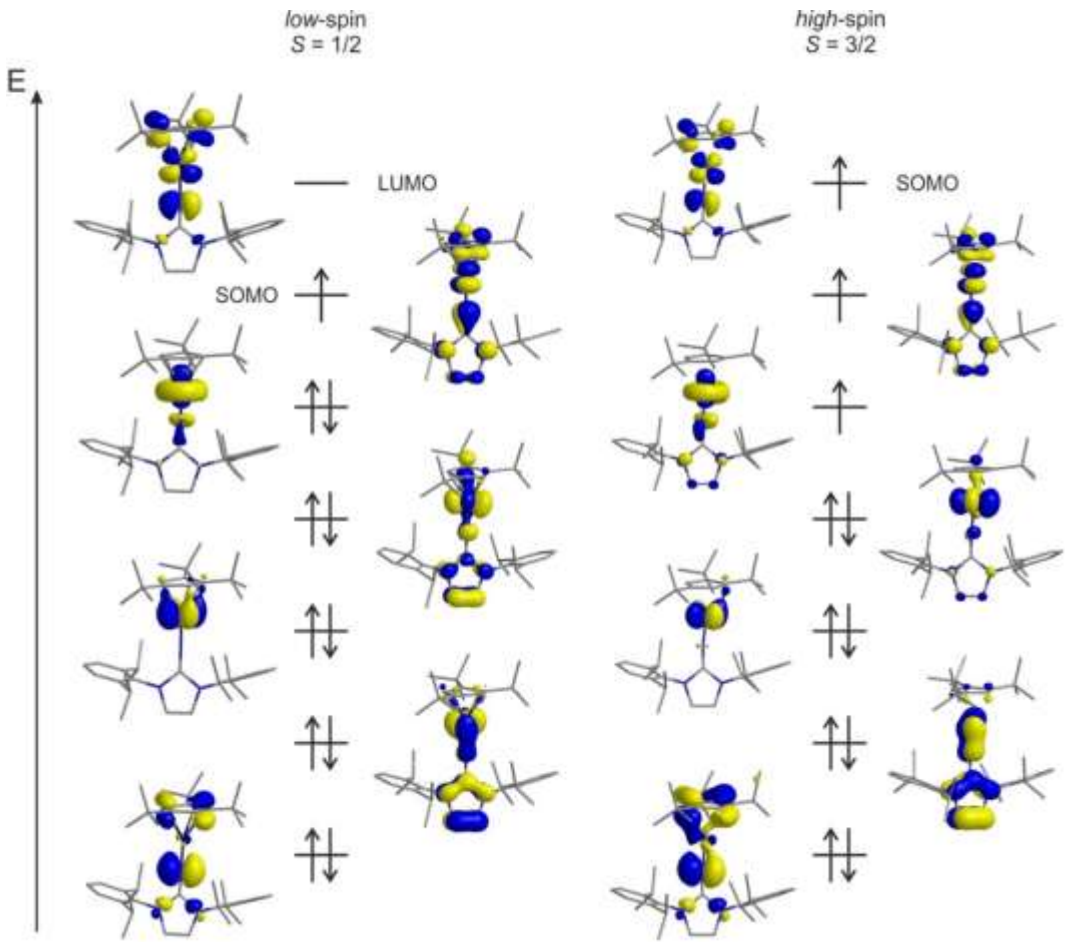

Figure S36. Biorthogonalized Kohn-Sham frontier orbitals on the B3LYP/6-311G(d,p) level of theory for complex **2-Co** (isosurface = 0.45).

S10 References

[1] Schneider, J.J; Czap, N.; Spickermann, D.; Lehmann, C. W.; Fontani, M.; Laschi. F.; Zanello, P., Synthesis, structure and spectroelectrochemistry of bis(η^6-1,4-tri-tert-butyl-benzene)chromium(0) and bis(η^5-1,2,4-tri-tert-butyl-cyclopentadienyl)cobalt(II). Dia- and paramagnet-ic sandwich complexes derived from sterically highly demanding π-ligands, *J. Organomet Chem.* **1999**, *590*, 7-14.

[2] Rigaku Oxford Diffraction, CrysAlisPRO Software System, Rigaku Corporation, Oxford, UK.

[3] Sheldrick, G. M., SHELXT – Integrated space-group and crystal-structure determination, *Acta Cryst.* **2015**, *A71*, 3-8.

[4] Sheldrick, G. M., Crystal structure refinement with SHELXL, *Acta Cryst.*, **2015**, *C71*, 3-8.

[5] Dolomanov, O. V.; Bourhis, L. J.; Gildea, R. J.; Howard, J. A. K.; Puschmann, H., OLEX2: a complete structure solution, refinement and analysis program, *J. Appl. Cryst.* **2009**, *42*, 339-341.

[6] Farrugia, L. J.; WinGX and ORTEP for Windows: an update, *J. Appl. Cryst.* **2012**, *45*, 849-854.

[7] Sheldrick, G. M., A short history of SHELX, *Acta Cryst.* **2008**, *A64*, 112-122.

[8] Bruker AXS, Madison, Wisconsin, USA.

[9] Walter, M. D.; Schultz, M.; Andersen, R. A., Weak paramagnetism in compounds of the type Cp'_2Yb(bipy), *New. J. Chem.* **2006**, *30*, 238-246.

[10] Bain, G. A.; Berry, J. F., Diamagnetic Corrections and Pascal's Constants, *J. Chem. Educ.* **2008**, *85*, 532-536.

[11] *julX Simulation of molecular magnetic data*; Bill, E.: Mühlheim an der Ruhr, 2014.

[12] Stoll, S.; Schweiger, A., EasySpin, a comprehensive software package for spectral simulation and analysis in EPR, *J. Magn. Reson.* **2006**, *178*, 42-55.

[13] Makinen, M. W.; Kuo, L.C.; Yim, M. B.; Wells, G. B.; Fukuyama, J. M.; Kim, J. E. Ground term splitting of high-spin cobalt(2+) ion as a probe of coordination structure. 1. Dependence of the splitting on coordination geometry, *J. Am. Chem. Soc.* **1985**, *107*, 5245-5255

[14] Park, J. S.; Park, T.-J.; Kim, K. H.; Oh, K.; Seo, M.-S.; Lee, H.-I.; Jun, M.-J.; Nam, W.; Kim, K. M.; Synthesis and Characterization of High-Spin Cobalt(II)-Based "Inorgainc Tennis Ball", *Bull. Korean Chem. Soc.* **2006**, *27*, 193-194

[15] Blume, M.; Tjon, J. A., Mössbauer Spectra in a Fluctuating Environment, *Phys. Rev.* **1968**, *165*, 446-456.

[16] Lagerec, K.; Rancourt, D. G., RECOIL Mössbauer Spectral Analysis Software for Windows, Version 1.02, Department of Physics, University of Ottawa, Ottawa, ON, **1998**.

[17] Wolfram Mathematica, Version 8.0.1.0, Wolfram Research Inc., February **2011**.

[18] Greenwood, N. N.; Gibb, T. C. (Eds.), „Mössbauer Spectroscopy", Chapman and Hall Ltd London, **1971**.

[19] Goldanskii, V. I.; Herber, R. H. (Eds.), „Chemical Applications of Mössbauer Spectroscopy", Academic Press New York and London, **1968**.

[20] a) Lee, C.; Yang W.; Parr, R. G.; Development of the Colle-Salvetti correlation-energy formula into a functional of the electron density, *Phys. Rev. B* **1988**, *37*, 785–789; b) Becke, A. D. Density-functional thermochemistry. III. The role of exact exchange, *J. Chem. Phys.* **1993**, *98*, 5648–5652.

[21] Gaussian 09, Revision A.1, M. J. Frisch, G. W. Trucks, H. B. Schlegel, G. E. Scuseria, M. A. Robb, J. R. Cheeseman, G. Scalmani, V. Barone, B. Mennucci, G. A. Petersson, H. Nakatsuji, M. Caricato, X. Li, H. P. Hratchian, A. F. Izmaylov, J. Bloino, G. Zheng, J. L. Sonnenberg, M. Hada, M. Ehara, K. Toyota, R. Fukuda, J. Hasegawa, M. Ishida, T. Nakajima, Y. Honda, O. Kitao, H. Nakai, T. Vreven, J. A. Montgomery, Jr., J. E. Peralta, F. Ogliaro, M.

Bearpark, J. J. Heyd, E. Brothers, K. N. Kudin, V. N. Staroverov, R. Kobayashi, J. Normand, K. Raghavachari, A. Rendell, J. C. Burant, S. S. Iyengar, J. Tomasi, M. Cossi, N. Rega, J. M. Millam, M. Klene, J. E. Knox, J. B. Cross, V. Bakken, C. Adamo, J. Jaramillo, R. Gomperts, R. E. Stratmann, O. Yazyev, A. J. Austin, R. Cammi, C. Pomelli, J. W. Ochterski, R. L. Martin, K. Morokuma, V. G. Zakrzewski, G. A. Voth, P. Salvador, J. J. Dannenberg, S. Dapprich, A. D. Daniels, Ö. Farkas, J. B. Foresman,J. V. Ortiz, J. Cioslowski, and D. J. Fox, Gaussian, Inc., Wallingford CT, **2009**.
[22] Neese, F. The ORCA program system. *WIREs Comput. Mol. Sci.* 2012, *2*, 73– 78,